12-1-2013

Constraints On A Second Planet In The WASP-3 System

G. Maciejewski

A. Niedzielski

A. Wolszczan

G. Nowak

R. Neuhäuser

See next page for additional authors

Authors

G. Maciejewski, A. Niedzielski, A. Wolszczan, G. Nowak, R. Neuhäuser, J. N. Winn, B. Deka, M. Adamów, M. Górecka, M. Fernández, F. J. Aceituno, J. Ohlert, R. Errmann, M. Seeliger, D. P. Dimitrov, D. W. Latham, G. A. Esquerdo, L. McKnight, M. J. Holman, Eric L.N. Jensen, U. Kramm, T. Pribulla, S. Raetz, T. O.B. Schmidt, C. Ginski, S. Mottola, S. Hellmich, C. Adam, H. Gilbert, M. Mugrauer, G. Saral, V. Popov, and M. Raetz

CONSTRAINTS ON A SECOND PLANET IN THE WASP-3 SYSTEM[*]

G. Maciejewski[1], A. Niedzielski[1], A. Wolszczan[2,3], G. Nowak[1], R. Neuhäuser[4], J. N. Winn[5], B. Deka[1], M. Adamów[1],
M. Górecka[1], M. Fernández[6], F. J. Aceituno[6], J. Ohlert[7,8], R. Errmann[4,9], M. Seeliger[4], D. Dimitrov[10],
D. W. Latham[11], G. A. Esquerdo[11], L. McKnight[5], M. J. Holman[11], E. L. N. Jensen[12], U. Kramm[13],
T. Pribulla[14], St. Raetz[4], T. O. B. Schmidt[4], Ch. Ginski[4], S. Mottola[15], S. Hellmich[15], Ch. Adam[4],
H. Gilbert[4], M. Mugrauer[4], G. Saral[11,16], V. Popov[10], and M. Raetz[17]

[1] Centre for Astronomy, Faculty of Physics, Astronomy and Informatics, Nicolaus Copernicus University, Grudziadzka 5, 87-100 Torun, Poland
[2] Department of Astronomy and Astrophysics, The Pennsylvania State University, 525 Davey Laboratory, University Park, PA 16802, USA
[3] Center for Exoplanets and Habitable Worlds, The Pennsylvania State University, 525 Davey Laboratory, University Park, PA 16802, USA
[4] Astrophysikalisches Institut und Universitäts-Sternwarte, Schillergässchen 2–3, D-07745 Jena, Germany
[5] Department of Physics, Massachusetts Institute of Technology, Cambridge, MA 02139, USA
[6] Instituto de Astrofísica de Andalucía (IAA-CSIC), Glorieta de la Astronomía 3, E-18008 Granada, Spain
[7] Michael Adrian Observatorium, Astronomie Stiftung Trebur, D-65468 Trebur, Germany
[8] University of Applied Sciences, Technische Hochschule Mittelhessen, D-61169 Friedberg, Germany
[9] Abbe Center of Photonics, Max-Wien-Platz 1, D-07743 Jena, Germany
[10] Institute of Astronomy, Bulgarian Academy of Sciences, 72 Tsarigradsko Chausse Blvd., 1784 Sofia, Bulgaria
[11] Harvard-Smithsonian Center for Astrophysics, 60 Garden Street, Cambridge, MA 02138, USA
[12] Department of Physics and Astronomy, Swarthmore College, Swarthmore, PA 19081, USA
[13] Institut für Physik, University Rostock, D-18051 Rostock, Germany
[14] Astronomical Institute, Slovak Academy of Sciences, 059 60 Tatranská Lomnica, Slovakia
[15] German Aerospace Center (DLR), Rutherfordstraße 2, D-12489 Berlin, Germany
[16] Astronomy and Space Sciences Department, Istanbul University, 34116 Fatih Istanbul, Turkey
[17] Private observatory, Stiller Berg 6, D-98587 Herges-Hallenberg, Germany

ABSTRACT

There have been previous hints that the transiting planet WASP-3b is accompanied by a second planet in a nearby orbit, based on small deviations from strict periodicity of the observed transits. Here we present 17 precise radial velocity (RV) measurements and 32 transit light curves that were acquired between 2009 and 2011. These data were used to refine the parameters of the host star and transiting planet. This has resulted in reduced uncertainties for the radii and masses of the star and planet. The RV data and the transit times show no evidence for an additional planet in the system. Therefore, we have determined the upper limit on the mass of any hypothetical second planet, as a function of its orbital period.

Key words: planetary systems – planets and satellites: individual (WASP-3b) – stars: individual (WASP-3)

Online-only material: supplemental data

1. INTRODUCTION

The extrasolar planetary system WASP-3 comprises a transiting planet with a mass of 1.7 times the mass of Jupiter ($M_{\rm Jup}$), which orbits a main-sequence star of spectral type F7–8 and apparent magnitude $V = 10.6$ (Pollacco et al. 2008). The orbital period is only 1.85 days, making WASP-3b one of the hottest planets known at the time of its discovery. The planetary radius, which is known to be 1.3 times larger than the radius of Jupiter ($R_{\rm Jup}$), is consistent with atmospheric models for strongly irradiated giant planets.

The system properties have been determined through several photometric and spectroscopic follow-up studies. Gibson et al. (2008), Tripathi et al. (2010), and Christiansen et al. (2011) acquired high-precision transit light curves and redetermined the stellar and planetary radii, orbital inclination, and transit ephemeris. The radial velocities (RVs) measured during transits exhibit the Rossiter–McLaughlin (RM) effect (Rossiter 1924;

McLaughlin 1924), in a pattern that indicates a low value for the sky-projected angle between the stellar spin axis and the planetary orbital axis (Simpson et al. 2010; Tripathi et al. 2010; Miller et al. 2010).

Tripathi et al. (2010) found that the measured mid-transit times seemed to be statistically inconsistent with strict periodicity, i.e., fitting the measured times to a linear function of epoch gave an unacceptably large χ^2. They noted that this could be explained as a consequence of either variations in the planetary orbit due to an unseen companion, or underestimated uncertainties in the measured mid-transit times. Maciejewski et al. (2010) measured six mid-transit times from light curves acquired with 0.6 m class telescopes, combined them with data from the literature, and concluded that the transit times may be modulated with a period of ∼127 days and a peak-to-peak amplitude of ∼4 minutes. Numerical simulations showed that such a pattern of transit timing variation (TTV) could be produced by an additional low-mass planet. The postulated TTV signal has not been confirmed by further observations (Littlefield 2011; Sada et al. 2012; Nascimbeni et al. 2013; Montalto et al. 2012), and analyses of the mid-transit times now exclude the originally postulated periodic TTV signal (Nascimbeni et al. 2013; Montalto et al. 2012). However, Nascimbeni et al. (2013) showed that the measured mid-transit times are still not statistically consistent with a linear ephemeris, and pointed out that

Table 1
Observed Transits and Light-curve Features

No.	Date UT	E	Telescope	Filter	Airmass	Weather	Γ	pnr	Templ.
1	2009 Sep 24	517	FLWO 1.2 m	i'	$1.02 \rightarrow 1.75$	Clear	1.36	1.40	✓
2	2010 May 25	649	Rozhen 0.6 m	I_C	$1.39 \rightarrow 1.01$	Clear	1.82	1.94	
3	2010 Jun 7	656	Rozhen 2.0 m	I_C	$1.58 \rightarrow 1.02$	Clear	1.77	1.24	✓
			Rozhen 0.6 m	I_C	$1.51 \rightarrow 1.01$	Clear	0.95	2.35	
4	2010 Jun 15	660	FLWO 1.2 m	r'	$1.88 \rightarrow 1.00$	Clear	1.54	0.99	✓
			Swarthm. 0.6 m	I_C	$1.06 \rightarrow 1.00 \rightarrow 1.15$	Clear	0.52	1.77	
5	2010 Jun 18	662	Ankara 0.4 m	R_C	$1.24 \rightarrow 1.00 \rightarrow 1.21$	Clear	4.60	2.52	
6	2010 Jun 26	666	FLWO 1.2 m	r'	$1.14 \rightarrow 1.00 \rightarrow 1.45$	Partly cloudy	1.36	1.15	✓
7	2010 Jul 9	673	Swarthm. 0.6 m	I_C	$1.06 \rightarrow 1.00 \rightarrow 1.65$	Clear	1.02	2.09	
8	2010 Jul 24	681	CAO 2.2 m	R_C	$1.00 \rightarrow 1.71$	Clear	1.28	1.12	✓
9	2010 Aug 5	688	CAO 2.2 m	R_C	$1.00 \rightarrow 1.59$	Clear	1.22	1.14	✓
10	2010 Aug 28	700	Swarthm. 0.6 m	I_C	$1.00 \rightarrow 2.08$	Clear	1.36	2.79	
11	2010 Aug 29	701	CAO 2.2 m	R_C	$1.05 \rightarrow 2.91$	Cirrus clouds	1.46	1.64	✓
12	2010 Sep 11	708	CAO 2.2 m	R_C	$1.01 \rightarrow 1.68$	Clear	1.71	1.28	✓
			Trebur 1.2 m	R_B	$1.08 \rightarrow 1.94$	Clear	2.14	1.24	✓
13	2011 Apr 3	818	Jena 0.9 m	R_B	$2.09 \rightarrow 1.08$	Clear	0.83	3.39	
14	2011 May 9	838	Jena 0.9 m	R_B	$1.75 \rightarrow 1.04$	Clear	1.05	2.86	
15	2011 May 17	842	FLWO 1.2 m	i'	$1.23 \rightarrow 1.00 \rightarrow 1.02$	Clear	1.36	0.94	✓
16	2011 Jun 3	851	Trebur 1.2 m	R_B	$1.23 \rightarrow 1.03 \rightarrow 1.04$	Clear	2.14	1.32	✓
17	2011 Jun 6	869	Swarthm. 0.6 m	r'	$1.01 \rightarrow 1.00 \rightarrow 1.31$	Clear	0.81	2.72	
18	2011 Jun 15	858	OSN 1.5 m	R_C	$1.62 \rightarrow 1.02$	Clear	2.73	1.43	✓
19	2011 Jun 27	864	Trebur 1.2 m	R_B	$1.05 \rightarrow 1.03 \rightarrow 1.17$	Clear	2.39	1.24	✓
20	2011 Jul 22	878	Ankara 0.4 m	R_C	$1.09 \rightarrow 1.00 \rightarrow 1.26$	Clear	4.63	2.67	
21	2011 Aug 2	884	Trebur 1.2 m	R_B	$1.03 \rightarrow 1.38$	Partly cloudy	1.82	1.43	
22	2011 Aug 14	890	OSN 1.5 m	R_C	$1.04 \rightarrow 2.64$	Clear	2.00	1.53	✓
23	2011 Aug 26	897	OSN 1.5 m	R_C	$1.01 \rightarrow 2.00$	Clear	1.11	2.49	
			CAO 1.2 m	R_C	$1.00 \rightarrow 2.08$	Clear	1.33	1.85	
24	2011 Sep 8	904	OSN 1.5 m	R_C	$1.01 \rightarrow 1.64$	Clear	2.14	1.46	✓
25	2011 Oct 2	917	OSN 1.5 m	R_C	$1.05 \rightarrow 2.14$	Clear	3.53	1.04	✓
			Trebur 1.2 m	R_B	$1.13 \rightarrow 2.39$	Partly cloudy	1.82	1.80	
			Jena 0.9 m	R_B	$1.13 \rightarrow 2.82$	Clear	1.29	2.76	
26	2011 Oct 15	924	Herg.-Hall. 0.2 m	Clear	$1.08 \rightarrow 1.88$	Clear	0.62	3.44	

Notes. Date UT is given for a mid-transit time, epoch E is a transit number from the initial ephemeris given in Pollacco et al. (2008), R_C and R_B denote Cousins and Bessell R-band filters, respectively, Γ is a median number of exposures per minute, and pnr is a photometric scatter in millimag per minute (see Section 2.1 for details). Light curves that were used to produce a transit template are marked with ✓ in the last column (Templ.).

such apparently chaotic timing variations could be produced by some specific orbital configurations. Montalto et al. (2012) suggested that chromospheric activity of the parent star could be a potential source of the transit timing noise.

In this paper we present results of new photometric and spectroscopic follow-up observations, the goal of which was to confirm or refute the hypothesis about the second planet in the WASP-3 system. As our newly measured mid-transit times are consistent with a linear ephemeris, and no signal in RV residuals from a single planet orbital fit is detected, we determine upper limits on the mass of a hypothetical second planet as a function of its orbital period. In addition, we redetermined the stellar and planetary properties of the WASP-3 system using our spectroscopic and photometric data sets.

2. OBSERVATIONS AND DATA REDUCTION

2.1. Transit Photometry

Twenty-six transits of WASP-3b were observed between 2009 September and 2011 October. Four of these transits were observed with two different telescopes, and one of the transits was observed with three different telescopes, giving a total of 32 light curves. Most of these data were collected with telescopes with diameters greater than 1 m, enabling

a photometric precision better than 1.5 mmag. A portion of the data was obtained in collaboration with the Young Exoplanet Transit Initiative (Neuhäuser et al. 2011). Individual observations are summarized in Table 1, and the light curves are plotted in Figure 1.[18] Short descriptions of the instrumental set-up and the observations are given below, arranged in descending order of telescope aperture size.

Four complete transits were observed in 2010 with the 2.2 m telescope at the Calar Alto Observatory (CAO, Spain) within the program H10-2.2-010. For the detector, we used the Calar Alto Faint Object Spectrograph in its imaging mode. The full field of view (FoV) was windowed to record the target star and nearby bright comparison star. Binning of 2×2 was applied to shorten the readout time. The optical set-up was significantly defocused to reduce the impact of flat-fielding imperfections. The telescope was autoguided to hold stellar images fixed on the same pixels throughout each night. The weather conditions on 2010 August 29 were non-photometric due to thin clouds, leading to reduced quality of the time-series photometry. During the other nights the sky was mainly clear but not perfect enough to achieve sub-millimagnitude precision. The gaps in light curves on 2010 August 5 and September 11 were caused by passing clouds.

---

[18] The photometric data are available at http://ttv.astri.umk.pl.
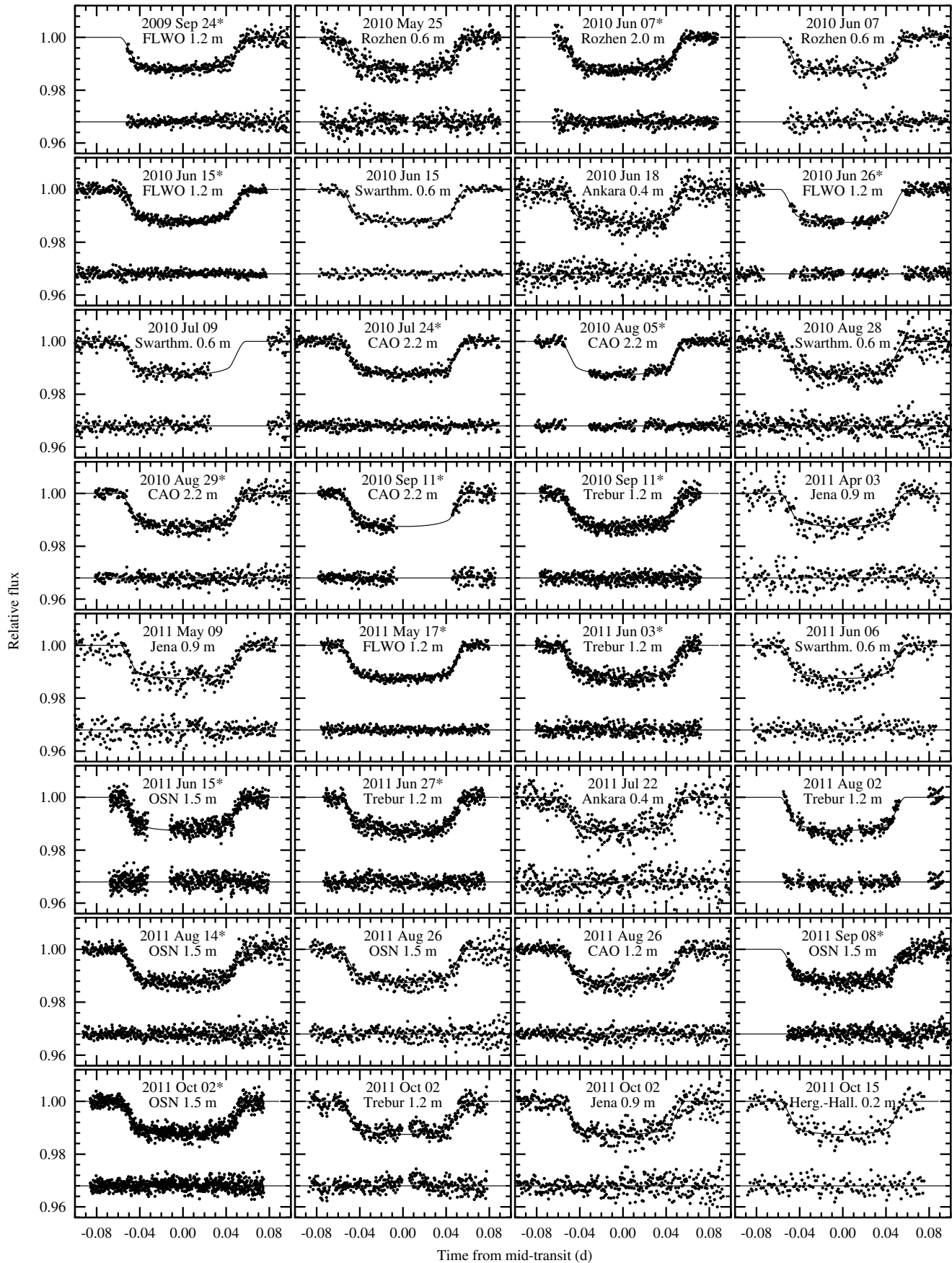
Figure 1. Transit light curves obtained for WASP-3b. Three-point binning was applied for light curves acquired at the Ankara University Observatory for clarity. Light curves that were used to produce a transit template are marked with an asterisk in the date of observation.

(Supplemental data for this figure are available in the online journal.)

The 2.0 m Ritchey–Chrétien–Coudé telescope at the Bulgarian National Astronomical Observatory Rozhen was used to observe a transit on 2010 June 7. The detector was a Roper Scientific VersArray 1300B CCD camera (1340 × 1300 pixels, FoV: 5′.8 × 5′.6).

Observations of five transits were carried out in 2011 with the 1.5 m telescope at the Sierra Nevada Observatory (OSN) operated by the Instituto de Astrofísica de Andalucía (Spain). A Roper Scientific VersArray 2048B CCD camera (2048 × 2048 pixels, FoV: 7′.92 × 7′.92) was used as a detector. The observations on 2011 June 15 were interrupted by technical failures. The lower-quality data from 2011 August 26, especially at the end of the run, were a consequence of observing through a large airmass.

The 1.2 m Trebur Telescope at the Michael Adrian Observatory in Trebur (Germany) was used to observe a transit in 2010 and four events in 2011. The Cassegrain-type telescope is equipped with a 3072 × 2048 pixel SBIG STL-6303 CCD camera (FoV: 10′.0 × 6′.7). A 2 × 2 binning mode was used.

Four transits were observed with the 1.2 m telescope at the Fred Lawrence Whipple Observatory (FLWO, USA). The detector was the Keplercam CCD system (4096 × 4096 pixels, binned 2 × 2, FoV: 23′ × 23′). The observations on 2010 June 26 were interrupted by occasionally passing clouds.

Observations of a transit on 2011 August 26 were conducted with the 1.23 m telescope at CAO. A CCD camera equipped with an e2v CCD231-84-NIMO-BI-DD sensor (4096 × 4096 pixels) was used, providing a 12′.5 × 11′.5 FoV.

The 0.9/0.6 m Schmidt Telescope at the University Observatory Jena in Großschwabhausen near Jena (Germany), equipped with the CCD imager Schmidt Teleskop Kamera (STK; Mugrauer & Berthold 2010, FoV: 52′.8 × 52′.8), was used to observe three transits. All light curves were acquired with clear sky, but some portion of the data was affected by adverse weather conditions (haze and high humidity).

Four light curves were taken at the Peter van de Kamp Observatory at Swarthmore College (Swarthmore, PA, USA) with a 0.6 m, $f/7.8$ Ritchey–Chrétien telescope and an Apogee U16M CCD (4096 × 4096 9 μm pixels, FoV: 26′ × 26′). The telescope was autoguided, which allowed each star's center of light to remain on the same location of the CCD within about 3–4 pixels over the course of a night.

The 0.6 m Cassegrain photometric telescope at Rozhen, equipped with an FLI PL09000 CCD camera (3056 × 3056 pixels, FoV: 17′ × 17′) was used to observe two transits in 2010.

A 0.4 m Schmidt–Cassegrain Meade LX200 GPS telescope at the Ankara University Observatory (Turkey) was employed to acquire two transit light curves. An Apoge ALTA-U47 CCD camera (1024 × 1024 pixels, FoV: 11′ × 11′) was used as a detector.

In addition, a transit on 2011 October 1 was taken with an 8 inch Schmidt–Cassegrain telescope and a G2-1600 CCD camera from Moravian Instruments Inc. (FoV: 48′ × 32′) at a private amateur observatory in Herges–Hallenberg (Germany).

Data reduction was based on standard procedures including debiasing, dark correction, and flat-fielding using sky flats. Differential photometry was performed with respect to the comparison stars available in each FoV. The aperture size was optimized to achieve the smallest scatter in the resulting out-of-transit light curves. The light curves were detrended by fitting a second-order polynomial function of time along with a trial transit model, using initial parameters obtained from the literature. This procedure was performed with the JKTEBOP code

Table 2
New Radial Velocities for the WASP-3 System

BJD$_{TDB}$	RV (m s^{-1})	Error (m s^{-1})
2455345.782701	195.802	36.312
2455349.755560	−6.370	41.495
2455350.765352	−71.253	30.760
2455365.710214	92.082	36.094
2455365.932853	238.030	40.097
2455369.705307	196.649	37.140
2455371.682112	186.664	28.075
2455372.681765	−262.104	38.049
2455806.729146	−243.796	31.687
2455807.742803	−9.394	54.541
2455810.717317	−1.821	33.684
2455812.716356	117.557	37.807
2455816.704736	93.935	32.336
2455823.683879	76.051	33.085
2455824.679898	−301.463	33.483
2455828.659585	−409.340	36.002
2455829.669701	180.807	41.666

Notes. Times are given for a middle of exposure as BJD based on TDB. RV values are relative to the mean value representative for a whole data set. All values are intentionally left unrounded.

(Southworth et al. 2004a, 2004b), which allows photometric trends to be modeled as polynomials up to fifth order. The best-fitting trend is subtracted from each light curve. Magnitudes are transformed into fluxes and normalized to have a mean of unity outside of the transit. The timestamps were converted to barycentric Julian dates in barycentric dynamical time (BJD$_{TDB}$; Eastman et al. 2010). To quantify the quality of each light curve, we used the photometric noise rate (pnr) defined as

$$\mathrm{pnr} = \frac{\mathrm{rms}}{\sqrt{\Gamma}}, \tag{1}$$

where the root mean square of the residuals, rms, is calculated from the light curve and a fitted model, and Γ is the median number of exposures per minute (Fulton et al. 2011).

2.2. Doppler Measurements

Seventeen precise RV measurements were acquired in 2010 and 2011 with the Hobby–Eberly Telescope (HET; Ramsey et al. 1998) located in the McDonald Observatory (USA). The High Resolution Spectrograph (HRS; Tull 1998) was used with $R = 60,000$ resolution. Data reduction was performed with the custom-developed ALICE code (Nowak et al. 2013). It employs the standard iodine cell method and cross-correlation technique to calibrate data and measure the velocities. Using the I$_2$ cell method to measure RVs independently in 96 pixel long segments of our HET/HRS spectra, we obtained information about the imperfections in the initial Th–Ar dispersion curve and determine the instrumental profile. With this information, we cleaned the iodine lines from our spectra and constructed the cross-correlation function from exactly the same parts of the spectra from which we measure RVs. For each epoch, the final value of the RV was taken to be the mean of the measurements from all 17 echelle orders. The measurement uncertainty was 28–42 m s^{-1} at the 1σ level. The new RVs are listed in Table 2.

Table 3
Parameters of the WASP-3 Star Derived from Spectroscopic Analysis

Parameter	This Work	Pol08	Mon12	Tor12
Effective temperature, $T_{\rm eff}$ (K)	6340 ± 90	6400 ± 100	6448 ± 123	6375 ± 63
Surface gravity, $\log g_*$ (cgs units)	4.25 ± 0.15	4.25 ± 0.05	4.49 ± 0.08	4.28 ± 0.03[a]
Metallicity, [Fe/H]	-0.161 ± 0.063	0.00 ± 0.20	-0.02 ± 0.08	-0.06 ± 0.08
Lithium abundance, A(Li) (dex)	2.65 ± 0.08	2.0–2.5		
Micro turbulent velocity, $v_{\rm mic}$ (km s^{-1})	1.4 ± 0.3			
Mass, M_* ($M_\odot$)	$1.11^{+0.08}_{-0.06}$	$1.24^{+0.06}_{-0.11}$		
Luminosity, L_* ($L_\odot$)	$2.4^{+0.4}_{-0.3}$			
Age (Gyr)	$3.9^{+1.3}_{-1.2}$	0.7–3.5		
Rotation velocity, $v \sin i$ (km s^{-1})	15.6 ± 1.5	13.4 ± 1.5	13.4–14.8	15.4 ± 1.2

Note. [a] Based on photometric analysis.
References. Pol08: Pollacco et al. 2008; Mon12: Montalto et al. 2012; Tor12: Torres et al. 2012.

3. RESULTS

3.1. Spectroscopic Parameters for the Host Star

To derive stellar properties, two spectra without iodine (acquired on 2010 May 29 and 2011 August 25) were combined to generate an averaged template spectrum. This template has a signal-to-noise ratio of 300. The first step was to measure the stellar rotation velocity $v \sin i$ with the cross-correlation technique as described by Nowak et al. (2013). The derived value of $v \sin i = 15.6 \pm 1.5$ km s^{-1} was used in further analyses. Then, we measured equivalent widths of iron lines with the Automatic Routine for line Equivalent widths in stellar Spectra (ARES; Sousa et al. 2007). These results were used to determine the atmospheric parameters. The data set was analyzed with the TGVIT code to determine the effective temperature $T_{\rm eff}$, surface gravity $\log g_*$, metallicity based on iron abundance [Fe/H], and micro turbulent velocity $v_{\rm mic}$. For a detailed description of the procedure, we refer the reader to Takeda et al. (2002, 2005).

In the next step, the obtained parameters were used to determine the stellar mass M_*, luminosity L_*, and age. We employed PARSEC isochrones in version 1.1 (Bressan et al. 2012) that were bilinearly interpolated to estimate the parameters and their uncertainties. The surface gravity is generally poorly constrained from spectroscopy (see Torres et al. 2012 and references therein). For transiting planetary systems this parameter can be replaced by a mean stellar density ρ_*, which is determined more accurately from the transit light curve analysis (see Section 3.3). In this approach, the mean stellar density is known independently of theoretical stellar models. A mean stellar density based on the values of $\log g_*$ and $T_{\rm eff}$ from spectroscopy in conjunction with the evolutionary models is in agreement with the value derived from the transit photometry. The final stellar parameters are listed in Table 3, and the position of WASP-3 in a modified Hertzsprung–Russell diagram is plotted in Figure 2.

We also used alternative methods to check the spectroscopic parameters obtained above. We pursued the photometric approach of Adamów et al. (2012), which is based on the $BVJHK_S$ photometry taken from the *Tycho*-2 catalog (Høg et al. 2000) and Two Micron All Sky Survey Point Source Catalog (Cutri et al. 2003). The effective temperature of 6280 ± 50 K was obtained from an empirical calibration of six colors by Ramírez & Meléndez (2005). A value of $\log g_* = 4.3$ was estimated from the empirical relation given by Straizys & Kuriliene (1981). A set of stellar parameters was also determined independently by spectrum modeling with the Spectroscopy Made Easy (SME)
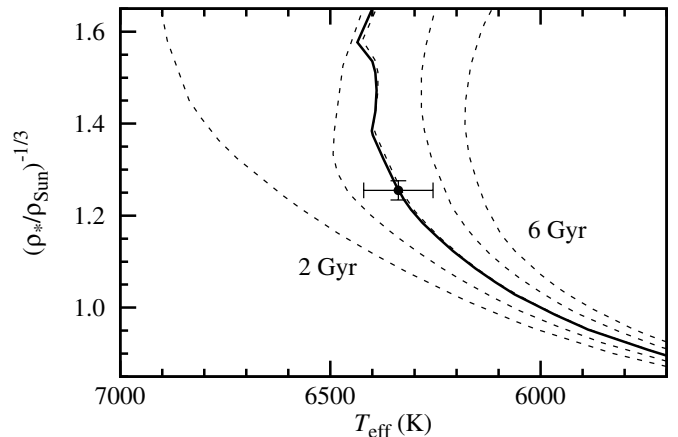

Figure 2. Position of WASP-3 (a central dot) in the modified Hertzsprung–Russel diagram. The PARSEC isochrones of the ages between 2 and 6 Gyr with a step of 1 Gyr are sketched with dashed lines. The best-fitting isochrone is drawn with a continuous line. Isochrones have been interpolated for redetermined iron abundance of [Fe/H] = -0.161.

code (Valenti & Piskunov 1996). The effective temperature was found to be 6440 K, $\log g_* = 4.3$, [Fe/H] = $+0.01$, and $v_{\rm mic} = 1.4$ km s^{-1}. Both methods gave results consistent with the values obtained with TGVIT.

The stellar parameters we have determined are in a perfect agreement with the values reported by Torres et al. (2012) and Pollacco et al. (2008), although we find a slightly less massive and less metal-rich host star ($M_* = 1.11^{+0.08}_{-0.06}$ $M_\odot$, [Fe/H] = -0.161 ± 0.063). The effective temperature and surface gravity we derived ($T_{\rm eff} = 6338 \pm 83$ K, $\log g_* = 4.255^{+0.040}_{-0.037}$ in cgs units) deviate only from values reported by Montalto et al. (2012). Those literature values are higher, although were obtained by reanalysis of archival spectra from Pollacco et al. (2008). Differences are probably caused by different methodologies. The lithium abundance of A(Li) = 2.65 ± 0.08 dex, measured from the Li I doublet at 6708 Å, is close to a range between 2.0 and 2.5 dex reported by Pollacco et al. (2008). It gives the system's age between 1.5 and 4 Gyr, based on an empirical relation obtained for open clusters (Sestito & Randich 2005). This estimate is consistent with the value of $3.9^{+1.3}_{-1.2}$ Gyr from isochrone fitting.

3.2. Stellar Activity

The typical spectroscopic stellar activity indicators, such as Ca II H (3968.47 Å) and K (3933.66 Å) lines and the infrared
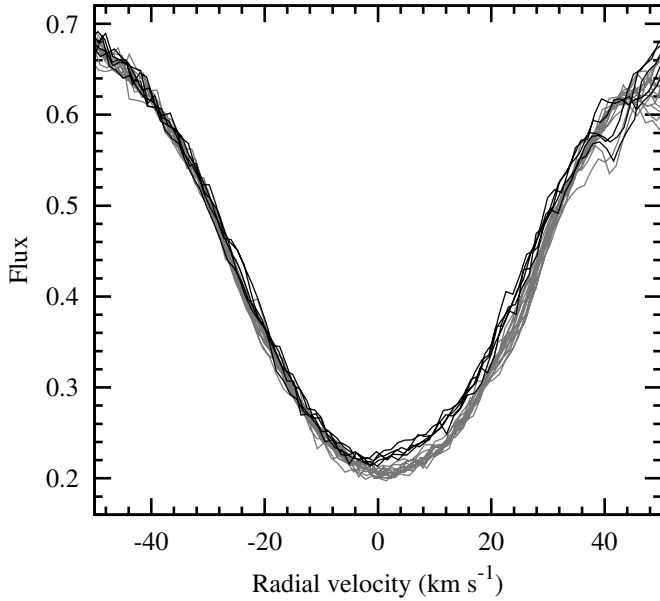
Figure 3. Stack of individual spectra centered on the Hα line and transformed into the RV domain. The spectra in a higher activity state are sketched with black lines, and those at the lower activity are drawn with gray lines. The profile becomes noticeably shallower and apparently blueshifted when the star is in the more active state.

Figure 4. Illustration of bands (grayed areas) used to determine the activity indices for the Hα and control Fe I 6593.884 Å lines. The bottom panels zoom in on bands centered on the investigated lines. The spectrum is a template for RV measurements (i.e., without I_2 lines) acquired on 2010 May 29.

Ca II triplet lines at 8498–8542 Å, are outside of the wavelength range of our spectra. Some alternative indicators, such as the Na I D1 (5895.92 Å), Na I D2 (5889.95 Å), and He I D3 (5875.62 Å) lines, are seriously contaminated by the I_2 lines. Therefore, we used the Hα (6562.808 Å) line as a chromospheric activity indicator. The variation in the shape of the Hα line between epochs can be seen in Figure 3. To create this figure the wavelengths based on the Th–Ar comparison lamp were transformed into RVs, after correcting for the barycentric Earth motion (using a procedure of Stumpff 1980), the absolute RV of the WASP-3, and the RV variation produced by the transiting planet (see Section 3.5).

The lines that were observed at epochs of higher activity are slightly shallower and blueshifted than the lines observed at epochs of lower activity. To quantify the stellar activity, we followed Gomes da Silva et al. (2012) and Robertson et al. (2013 and references therein). We determined the Hα index ($I_{H\alpha}$) as the ratio of the summed flux within a band of a width of 73 km s^{-1} (∼1.6 Å) centered on the core of the Hα line ($F_{H\alpha}$), and the summed flux within two reference bands ($F_1 + F_2$) on both sides of the Hα (between −1400 and −1000 km s^{-1} for F_1 and 1000 and 1400 km s^{-1} for F_2):

$$I_{H\alpha} = \frac{F_{H\alpha}}{F_1 + F_2}. \tag{2}$$

The adopted bands are illustrated in Figure 4. Values of the activity index were determined for 19 epochs, 17 listed in Table 2 and two template spectra taken in 2010 and 2011 that were used to determine precise RV measurements and stellar parameters. The uncertainties of $I_{H\alpha}$ were calculated adopting Equation (2) of Robertson et al. (2013):

$$\sigma_{I_{H\alpha}} = I_{H\alpha} \left(\left(\frac{\sigma_{F_{H\alpha}}}{F_{H\alpha}} \right)^2 + \left(\frac{\sqrt{\sigma_{F_1}^2 + \sigma_{F_2}^2}}{F_1 + F_2} \right)^2 \right)^{1/2}, \tag{3}$$
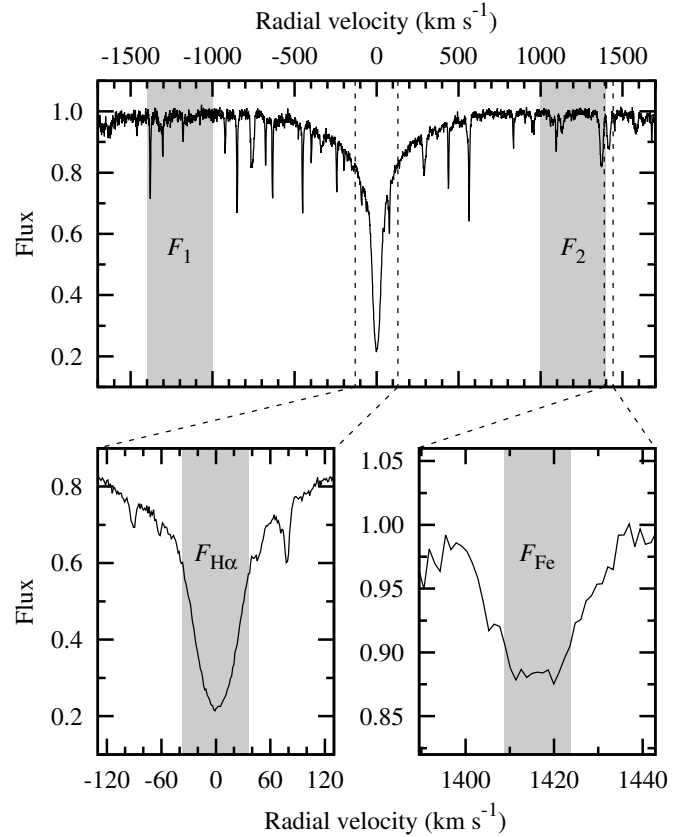
where $\sigma_{F_{H\alpha}}$ is the rms scatter in the continuum in the 0.5 Å adjacent to the investigated line multiplied by the square root of the number of pixels in the line, and σ_{F_1} and σ_{F_2} are the values of the rms scatter in the reference bands multiplied by the square root of the number of pixels in these bands.

To take possible instrumental effects into account, we also measured the index for the Fe I 6593.884 Å line (Molaro & Monai 2012), which is expected to be insensitive to stellar activity. We used a band of a width of 14.5 km s^{-1} (0.32 Å), centered on the core of the line, and the same reference bands (see Figure 4). As our stellar spectra were taken through the I_2 cell to precisely measure RVs, the wavelength regime relevant to our line indices may still contain weak I_2 lines (up to ∼4% relative to the continuum). Thus, we measured the Hα and Fe I indices for the iodine flat-field spectra. These indices show the rms variation at a level of 0.22% and 0.21% for the Hα and Fe I index, respectively. This intrinsic scatter is much smaller than the rms scatter for the stellar $I_{H\alpha}$ (2.39%) and I_{Fe} (0.58%). These findings show that the presence of the weak I_2 lines in the combined stellar-iodine spectra do not introduce significant errors into determinations of the activity indices.

As most of our HET/HRS observations were obtained during "priority 4" time (non-ideal moon phase and weather), we also searched for any variability in water vapor lines near the Hα wavelength regime. We measured the Hα and Fe I indices for very rapidly rotating and therefore line-depleted stars observed within the framework of the Pennsylvania-Toruń Search for Planets project (Niedzielski et al. 2011). Using 203 spectra of these stars, acquired between 2004 January and 2012 August, we
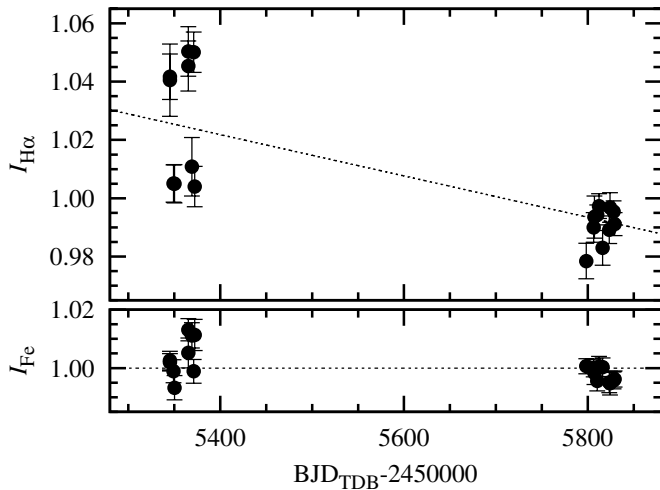
Figure 5. Activity indices determined for Hα (upper panel) and Fe I (bottom panel) lines as a function of time, normalized to the mean values for ease of comparison. Measurements grouped around 2455350 and 2455800 BJD were obtained in 2010 and 2011, respectively.

(Supplemental data for this figure are available in the online journal.)

found no seasonal (annual) variability of the telluric Hα and Fe I indices. Therefore, we conclude that neglecting the contribution of the telluric lines to the WASP-3 spectra does not introduce systematic errors in the determination of Hα and Fe I indices.

Figure 5 shows the behavior of $I_{H\alpha}$ and I_{Fe} (both normalized to their mean values) as a function of time. While I_{Fe} remains constant between the 2010 and 2011 observing seasons, there is a noticeable decrease of $I_{H\alpha}$. A linear regression gives a gradient of $\Delta I_{H\alpha} = (-2.3 \pm 0.5) \times 10^{-6}$ day^{-1}. Moreover, measurements in 2010 exhibit larger scatter, compared to the less active stage in 2011. This effect could be caused by slowly evolving active regions on the stellar surface, which are modulated by stellar rotation.

3.3. Transit Model

We selected a collection of the highest-quality light curves for modeling with the Transit Analysis Package[19] (TAP v2.1; Gazak et al. 2012) to obtain transit parameters. The selection was done iteratively. Light curves were sorted according to the pnr (see Section 2.1). The fitting procedure started with a few light curves with the smallest value of pnr and subsequent light curves were added in the next iterations. We noticed that including data sets with pnr > 1.64 mmag degraded the quality of the fit, so the procedure was interrupted, and finally a set of 16 best-quality light curves (indicated in Table 1 and Figure 1) was used to generate the transit model. Despite its relatively good value of pnr = 1.43 mmag, a light curve observed on 2011 August 2 was excluded because it is incomplete and exhibits the correlated noise which can be clearly seen in the residuals (Figure 1). The final sample comprises 11 light curves in the R band, two in r', two in i', and one in I. TAP uses the Markov Chain Monte Carlo (MCMC) method, with the Metropolis–Hastings algorithm and a Gibbs sampler, to find the best-fitting parameters based on the transit model of Mandel & Agol (2002). In estimating the parameter uncertainties, the wavelet-based technique of Carter & Winn (2009) is used to take into account time-correlated noise. It has been shown that this approach provides the most reliable parameters and error estimates (e.g., Hoyer et al. 2012).

The TAP code employs the quadratic limb-darkening (LD) law. As the initial values for the fitting procedure, we used theoretical values of LD coefficients (LDCs) from tables of Claret & Bloemen (2011), linearly interpolated with the EXOFAST applet[20] (Eastman et al. 2013) for the WASP-3 stellar parameters that were presented in Section 3.1. In the final iteration, the linear LDCs were allowed to vary freely. The quadratic terms were allowed to vary subject to Gaussian priors centered on the theoretical values, with a Gaussian width of 0.05. This approach is justified when data are not precise enough to solve for both the linear and quadratic LDCs. When both coefficients were allowed to vary, the fitting procedure sometimes gave unphysical results. We also considered a scenario in which the LDCs were held fixed at the theoretical values. This approach does not take into account any uncertainty in the LDCs, and the resulting parameter uncertainties were correspondingly reduced by up to 12%.

Three of the model parameters—the orbital inclination i_b, semimajor axis scaled by stellar radius a_b/R_*, and planetary to stellar radii ratio R_b/R_*—were required to be consistent across all of the light curves. The LDCs were also required to be the same for all of the data in a given bandpass. The orbital period was fixed at a value of 1.8468349 days, taken from Nascimbeni et al. (2013), and the mid-transit times of individual light curves were left as free parameters to account for possible timing variations. In addition, the fitting procedure accounted for the uncertainties in the linear trends in individual data sets that were removed at the preprocessing stage (Section 2.1). Since the RVs are consistent with a circular orbit (Section 3.5), we assumed in the transit analysis that the orbit of WASP-3b is perfectly circular.

Ten MCMC chains, each containing 10^6 steps, were computed. The individual chains were combined to get final posteriori probability distributions. The first 10% of the links in each chain were discarded before calculating the best-fitting parameter values and their uncertainties. They were determined by taking the median value of marginalized posteriori probability distributions, which were found to be unimodal. The 15.9 and 84.1 percentile values of the cumulative distributions were used to define the upper and lower 1σ uncertainties.

Table 4 gives the results, and compares them to other determinations in the literature. The optimized transit models for different filters are plotted in Figure 6. The values reported in this work agree with most of the previous determinations. Some of the comparisons are not straightforward because different methods have been used for parameter estimation; in particular, many of the previous determinations did not take time-correlated noise into account, and the reported uncertainties are likely to have been underestimated. Nevertheless, our more conservative determinations are generally more precise than most of those from previous studies. The linear LDCs of $u_R = 0.24 \pm 0.04$, $u_{r'} = 0.28 \pm 0.06$, and $u_{i'} = 0.18 \pm 0.06$ were found to be systematically smaller than the theoretical values ($u_R^t = 0.28$, $u_{r'}^t = 0.30$, and $u_{i'}^t = 0.23$), but within the uncertainties. The exception is $u_I = 0.23 \pm 0.10$ which was found to be slightly greater than the theoretical value of $u_I^t = 0.21$. This finding seems not to be conclusive because it is based on a single light curve which could be affected by imperfect detrending (there were few observations before the beginning of the transit). Interestingly, Nascimbeni et al. (2013), who fitted a linear LDC in the R band, also obtained a smaller value of u_R. These subtle

---

[19] http://ifa.hawaii.edu/users/zgazak/IfA/TAP.html

[20] http://astroutils.astronomy.ohio-state.edu/exofast/limbdark.shtml

Parameter	This Work	Pol08	Gib08	Chr11	Mon12	Nas13
Orbital inclination, i_b (degrees)	$84.15^{+0.41}_{-0.40}$	$84.4^{+2.1}_{-0.8}$	$85.06^{+0.16}_{-0.15}$	84.22 ± 0.81		84.12 ± 0.82
Scaled semimajor axis, a_b/R_*	$5.05^{+0.09}_{-0.09}$					
Planetary to stellar radii ratio, R_b/R_*	$0.10649^{+0.00061}_{-0.00063}$	$0.1030^{+0.0010}_{-0.0015}$	$0.1014^{+0.0010}_{-0.0008}$	0.1051 ± 0.0124	0.1061 ± 0.0007	0.1058 ± 0.0012
Transit parameter, $b = \frac{a_b}{R_*} \cos i_b$	$0.492^{+0.042}_{-0.041}$	$0.505^{+0.051}_{-0.166}$	$0.448^{+0.014}_{-0.014}$			
Linear LD coefficient in R, u_R	0.24 ± 0.04					$0.247^{+0.029}_{-0.028}$
Linear LD coefficient in I, u_I	0.23 ± 0.10					
Linear LD coefficient in r', $u_{r'}$	0.28 ± 0.06					
Linear LD coefficient in i', $u_{i'}$	0.18 ± 0.06					
Planetary radius, R_b ($R_{\rm Jup}$)	1.346 ± 0.063	$1.31^{+0.07}_{-0.14}$	$1.29^{+0.05}_{-0.12}$	1.385 ± 0.060		
Planetary density, ρ_b ($\rho_{\rm Jup}$)	$0.73^{+0.15}_{-0.14}$	$0.78^{+0.28}_{-0.09}$	$0.82^{+0.14}_{-0.09}$			
Planetary surface gravity, g_b (m s^{-2})	24 ± 2	$23.4^{+5.4}_{-2.1}$	$26.3^{+3.9}_{-2.3}$			
Stellar radius, R_* ($R_\odot$)	$1.298^{+0.053}_{-0.045}$	$1.31^{+0.05}_{-0.12}$	1.354 ± 0.056			
Stellar density, ρ_* ($\rho_\odot$)	$0.506^{+0.026}_{-0.025}$	$0.55^{+0.15}_{-0.05}$			0.57 ± 0.05	
Stellar surface gravity, $\log g_*$ (cgs units)	4.26 ± 0.04	$4.30^{+0.07}_{-0.03}$				

References. Pol08: Pollacco et al. 2008; Gib08: Gibson et al. 2008; Chr11: Christiansen et al. 2011; Mon12: Montalto et al. 2012; Nas13: Nascimbeni et al. 2013.
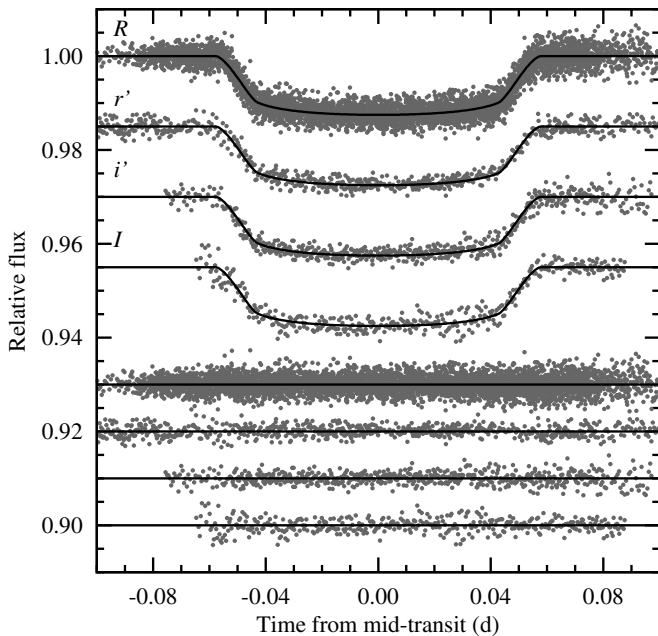

Figure 6. Composite light curves in individual filters with the best-fitting transit models. The residuals are plotted in the bottom.

differences between observed and theoretical values may be caused by imperfect LD tables or the presence of active areas on the stellar surface (Csizmadia et al. 2013). They could also be caused by biases related to transit fitting; for example, the LDCs determined from transit light curves have been found to depend on the transit parameter (Howarth 2011).

The fitting procedure was repeated with i_b, a_b/R_*, and R_b/R_* allowed to vary between individual epochs and individual filters to search for variations in these parameters with time and bands. The linear LDCs were allowed to vary around the values derived earlier, subject to a Gaussian prior defined by previously derived uncertainties. We found that none of the parameters show a periodic modulation or a long-timescale trend. These results cast into doubt the transit duration variation postulated by Eibe et al. (2012). Possible variations in R_b/R_* could be induced by stellar activity if the fraction of the stellar surface covered by spots changes from transit to transit (e.g., Carter et al. 2011). In addition, occultations of dark spots by a plan-

etary disk would produce apparent brightening in transit light curves (Schneider 2000; Silva 2003), which are not seen in any of the highest-quality data sets. There is therefore no purely photometric evidence for stellar activity. Moreover, no significant differences in R_b/R_* have been found between R, I, r', and i' filters.

3.4. Mid-transit Times

The transit model based on the best-quality data (Section 3.3) was used as a template to determine the mid-transit times for each individual light curve, using the TAP code. The parameters i_b, a_b/R_*, R_b/R_*, and the LDCs were allowed to vary, subject to Gaussian priors based on the results described previously. This approach guarantees that the uncertainties in the model parameters are taken into account in the error budget for each mid-transit time. For each individual light curve fit, the orbital period is of little consequence, but for completeness it was held fixed as in Section 3.3. The mid-transit time, as well as the flux slope and intercept, were taken to be free parameters. The MCMC analysis used 10 chains of a length of 10^5 steps for each light curve. Five transits were observed with more than one telescope. In such cases the light curves were fitted simultaneously to increase timing precision by up to 31%, depending on the quality of individual data sets. The results for the mid-transit times are listed in Table 5. They were combined with 53 published mid-transit times to refine the transit ephemeris. The mid-transit time from the discovery paper (Pollacco et al. 2008) was excluded because its value was determined as an average from various data sets. We used redetermined times by Nascimbeni et al. (2013), who performed a uniform analysis of all data sets available to those authors. We also used times reported by Eibe et al. (2012) and Montalto et al. (2012). As a result of a linear fit which uses individual timing errors as weights, we obtained the orbital period of $P_b = 1.8468351 \pm 0.0000004$ days and the time of transit at cycle zero of $T_0 = 2454143.85112 \pm 0.00024$ BJD$_{\rm TDB}$ with reduced $\chi^2 = 3.3$. We adopted the cycle numbering starting from the ephemeris given by Pollacco et al. (2008). The $O - C$ (observed minus calculated) diagram for transit timing is plotted in Figure 7.

The timing residuals (the observed mid-transit times after subtracting the best-fitting linear function of epoch number)
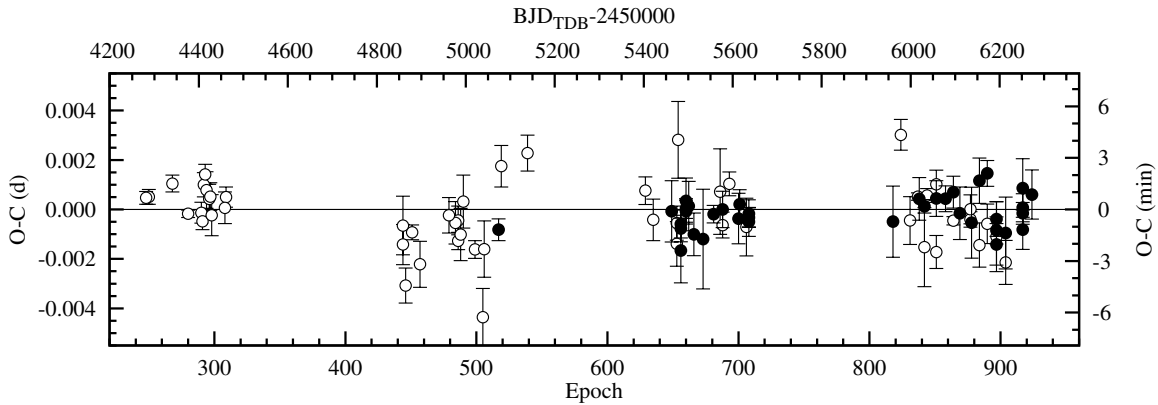
Figure 7. $O - C$ diagram for transit timing of WASP-3b. Open and filled symbols mark times from the literature and our new results, respectively.

Table 5
Mid-transit Times Determined for Individual Epochs

Date UT	N_{LC}	Epoch	T_{mid} (BJD$_{TDB}$)	$O - C$ (days)
2009 Sep 24	1	517	$2455098.66406 \pm 0.00044$	-0.00080
2010 May 25	1	649	2455342.4470 ± 0.0012	-0.0001
2010 Jun 7	2	656	$2455355.37419 \pm 0.00053$	-0.00075
2010 Jun 15	2	660	$2455362.76233 \pm 0.00040$	$+0.00005$
2010 Jun 18	1	662	2455366.4561 ± 0.0010	$+0.0002$
2010 Jun 25	1	666	$2455373.84230 \pm 0.00086$	-0.00099
2010 Jul 9	1	673	2455386.770 ± 0.0020	-0.0012
2010 Jul 24	1	681	$2455401.54564 \pm 0.00036$	-0.00017
2010 Aug 5	1	688	$2455414.47368 \pm 0.00073$	$+0.00002$
2010 Aug 28	1	700	2455436.6353 ± 0.0010	-0.0004
2010 Aug 29	1	701	2455438.4827 ± 0.0006	$+0.0002$
2010 Sep 11	2	708	2455451.4101 ± 0.0004	-0.0003
2011 Apr 3	1	818	2455654.5618 ± 0.0014	-0.0005
2011 May 9	1	838	$2455691.49938 \pm 0.00086$	$+0.00045$
2011 May 17	1	842	$2455698.88641 \pm 0.00027$	$+0.00015$
2011 Jun 3	1	851	$2455715.50824 \pm 0.00072$	$+0.00046$
2011 Jun 6	1	869	2455748.7507 ± 0.0011	-0.0001
2011 Jun 15	1	858	$2455728.43608 \pm 0.00052$	$+0.00045$
2011 Jun 27	1	864	$2455739.51735 \pm 0.00064$	$+0.00071$
2011 Jul 22	1	878	2455765.3718 ± 0.0014	-0.0005
2011 Aug 2	1	884	$2455776.45452 \pm 0.00092$	$+0.00118$
2011 Aug 14	1	890	$2455787.53583 \pm 0.00053$	$+0.00147$
2011 Aug 26	2	897	$2455800.46137 \pm 0.00055$	-0.00083
2011 Sep 8	1	904	2455813.3891 ± 0.0015	-0.0009
2011 Oct 2	3	917	$2455837.39876 \pm 0.00044$	-0.00014
2011 Oct 15	1	924	2455850.3274 ± 0.0010	$+0.0006$

Notes. Date UT is given for a mid-transit time, N_{LC} is the number of light curves used, epoch is the transit number from the initial ephemeris, T_{mid} is mid-transit time in BJD based on TDB, and $O - C$ is the timing deviation from the linear ephemeris.

were searched for any periodic variation using a Lomb–Scargle periodogram (Lomb 1976; Scargle 1982). The strongest peak was found to be insignificant, with a false alarm probability equal to 52%. This value was determined empirically by a bootstrap resampling method which generates 10^5 data sets with the randomly permuted $O - C$ values at the original observing epochs, and determines the fraction of resampled data sets with power higher than the original data set.

The value of reduced χ^2 for the linear ephemeris is far from unity. In principle this may be caused by a quasi-periodic or non-periodic (chaotic) TTV signal, or a long-timescale TTV signal. The first scenario is doubtful because the new

observations produce no significant peak in the periodogram of timing residuals. The detection of the putative TTV signal by Maciejewski et al. (2010) was probably caused by small-number statistics. The second possibility was pointed out by Nascimbeni et al. (2013) and it could be generated by a specific two-planet configurations close to mean-motion resonances or by configurations with more than one perturbing body. The third scenario, employing a parabolic fit reflecting any secular variation in the orbital period, has already been ruled out by Montalto et al. (2012). The high value of χ^2 could also be a simple consequence of underestimating the uncertainties in the mid-transit times. It has been shown that Monte Carlo, bootstrapping, or residual-shift (prayer-bead) methods may lead to underestimated uncertainties by a factor of up to four (see, e.g., Maciejewski et al. 2013). The wavelet-based techniques that are implemented in TAP allow one to take into account time-correlated noise in the photometric data, and seem to provide the most reliable uncertainty estimates (Carter & Winn 2009). Transit timing may also be affected by systematic effects caused by weather conditions (e.g., passing thin clouds, variable atmospheric extinction), instrumental factors (e.g., imperfect autoguiding, variable characteristic of the CCD matrix), or data reduction (e.g., detrending and normalization of a light curve). These effects are difficult to account for in the error budget, and may generate outliers in the $O - C$ diagram. If the sample of transit times is limited to those reported in this paper and two points reported by Gibson et al. (2008; taken for a longer timespan), the reduced χ^2 for a linear ephemeris is equal to 1.07. This result shows that our transit times are consistent with the linear ephemeris. We also examined those light curves which are the sources of mid-transit times lying more than 1σ away from zero in the $O - C$ diagram (note that no point deviates by more than 3σ). Most of these light curves have incomplete coverage of a transit or were obtained on nights with variable conditions (thin clouds, deteriorating transparency, or a high airmass range). Thus, we conclude that the large scatter in the $O - C$ diagram is likely a consequence of underestimated uncertainties due to observational and/or data-analysis factors.

3.5. Orbital Fit

The Systemic Console software (Meschiari et al. 2009) was used to refine the orbital parameters of WASP-3b. The data from Pollacco et al. (2008), Tripathi et al. (2010), and Simpson et al. (2010) were combined with our new RV measurements to derive the planet's minimum planetary mass $M_b \sin i_b$ and semimajor axis a_b. Pollacco et al. (2008) and Simpson et al.

Parameter	This Work	Pol08	Mon12
RV semi-amplitude, k (m s^{-1})	272 ± 10	$251.2^{+7.9}_{-10.8}$	277–290
Semimajor axis, a_b (AU)	$0.0305^{+0.0008}_{-0.0006}$	$0.0317^{+0.0005}_{-0.0010}$	
Minimum planetary mass, $M_b \sin i_b$ ($M_{\rm Jup}$)	$1.76^{+0.11}_{-0.09}$		
Planetary mass, M_b ($M_{\rm Jup}$)	$1.77^{+0.11}_{-0.09}$	$1.76^{+0.08}_{-0.14}$	

References. Pol08: Pollacco et al. 2008; Mon12: Montalto et al. 2012.

(2010) reported RV measurements obtained with the SOPHIE spectrograph on the 1.9 m telescope at the Observatoire de Haute Provence. Tripathi et al. (2010) used the High Resolution Echelle Spectrometer on the Keck I Telescope at the W. M. Keck Observatory on Mauna Kea to study the RM effect and to refine the orbital parameters. The data points that were obtained during transits (± 80 minutes from the expected mid-transit time, based on the transit ephemeris refined in Section 3.4) were removed from the sample because our orbital model does not account for the RM effect. In the fitting procedure, the RV offsets between individual instruments were allowed to vary to account for differences in the calibration of system velocities. The mid-transit times after 3σ clipping were included in the RV model to better constrain the mean anomaly at an initial epoch. The orbital period was allowed to be a free parameter, in order to verify the value obtained from transit timing alone, and to take into account the uncertainty in the orbital period when computing the uncertainties in the other parameters. For this analysis we adopted the value of M_* with uncertainties obtained in Section 3.1.

The Nelder–Mead minimization algorithm was used to find the best-fitting Keplerian orbit solution. The MCMC method was used to determine parameter uncertainties. The MCMC chain was 10^6 steps long, and the first 10% of the configurations were discarded. The scale parameters were set empirically in a series of attempts to get the acceptance rate of the MCMC procedure close to the optimal value of 0.25. For each parameter, the standard deviation was taken as the final error estimate. Two scenarios with circular and eccentric orbits were considered. In the latter case, the eccentricity was found to be $e_b = 0.02 \pm 0.01$ with reduced χ^2 equal to 1.18 and rms$_{\rm rv}$ equal to 26.7 m s^{-1}. The circular-orbit model fits nearly as well as the eccentric-orbit model, with reduced $\chi^2 = 1.26$ and rms$_{\rm rv} = 27.5$ m s^{-1}. As the significance of the non-zero eccentricity is low and there is no significant improvement in RV residuals, we discard the non-circular solution and adopt $e_b = 0.0$ in subsequent calculations. This approach is also supported by observations of planetary occultations at the time expected for a circular orbit (Zhao et al. 2012). The orbital solution is illustrated in Figure 8 and the redetermined parameters are given in Table 6.

Our RV data set and that of Tripathi et al. (2010) contain measurements spanning two consecutive observing seasons. Splitting these data sets into individual seasons and keeping relative offsets as free parameters could reveal possible long-term RV shifts caused by instrumental effects, small-number statistics, stellar activity, or additional bodies on wide orbits. This approach results in the value of rms$_{\rm rv}$ reduced by 10%. However, the relative offsets were found to be 6 ± 16 and 40 ± 27 m s^{-1} for the data set of Tripathi et al. (2010) and our new measurements, respectively. Both values are consistent with zero within $\sim 1.5\sigma$. Therefore there is no compelling evidence for any RV trends over the timespan of 1 yr.
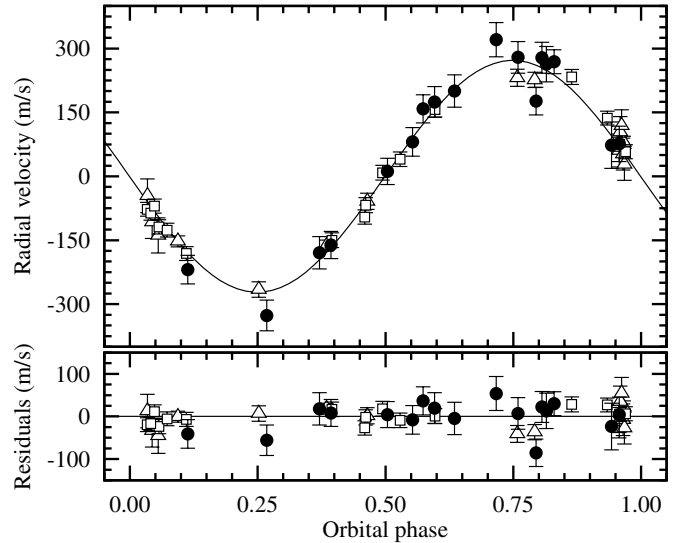

Figure 8. Phase-folded RV variations induced by the WASP-3 planet. Open triangles denote measurements from Pollacco et al. (2008) and Simpson et al. (2010). Open squares come from Tripathi et al. (2010). Our new data points are marked with filled circles. The best-fitting model assuming the circular orbit is sketched with a continuous line.

3.6. Constraints on an Additional Planet

The absence of any detectable periodic TTV signal, and the absence of any RV evidence for a departure from a single Keplerian orbit, allows us to place constraints on the properties of any hypothetical second planet in the system. The MERCURY 6 package (Chambers 1999) with the Bulirsch–Stoer integrator was used to generate a set of synthetic $O - C$ diagrams for WASP-3b in the presence of a fictitious perturbing planet. The mass of the fictitious planet was set at 0.5, 1, 5, 10, 50, 100, and 500 $M_{\rm Earth}$ (Earth masses), and the initial orbital distance varied between 0.006 and 0.2 AU with a step of 2×10^{-6} AU. The initial orbital longitude of WASP-3b was set at a value calculated for cycle zero, and the initial longitude of the fictitious planet was shifted by $180°$. The system was assumed to be coplanar, with both orbits initially circular. The integration time covered 1250 days, i.e., the time span of the transit observations. The value of rms was calculated for each synthetic $O - C$ diagram. Then, for each value of the orbital distance, we determined the range of planet masses for which the calculated rms$_{\rm ttv}$ was smaller than 80 s. Before calculating rms$_{\rm ttv}$, a 3σ clipping was applied to remove "outlying" data points. An upper mass of the fictitious planet at the detection limit was found by linear interpolation for masses below 500 $M_{\rm Earth}$. If rms$_{\rm ttv}$ was found to be generated by a more massive body, the limiting mass was extrapolated using a linear trend as fitted to 100 and 500 $M_{\rm Earth}$. Most of orbits located within ~ 3.5 Hill radii of WASP-3b (i.e., close to 1:1 orbital period commensurability) were found
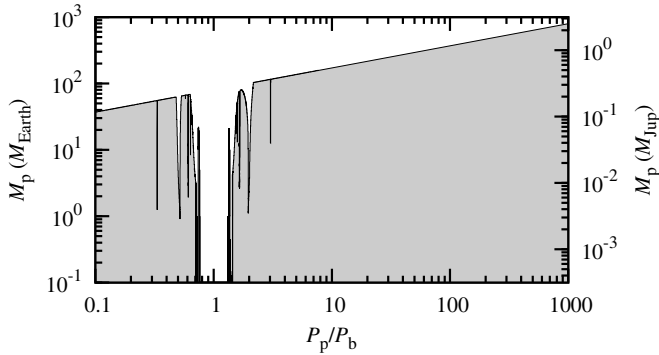
Figure 9. Upper mass limit for a fictitious second planet in the WASP-3 system, based on timing and RV data sets, as a function of an orbital period of that planet, P_p. The grayed area marks configurations that are below our detection threshold.

to be highly unstable and planetary close encounters or planet ejections occurred during the relatively short time of integration.

A similar approach was applied to the RV data set. The value of rms$_{rv}$ (Section 3.5) was used to calculate the mass limit as a function of the semimajor axis of the fictitious planet. Again, circular orbits were assumed. Then, both criteria were combined to obtain the upper mass limit of the possible second planet, based on transit timing and RV data sets. The results are plotted in Figure 9.

While the RV method gives tighter constraints for most configurations, the TTV technique is sensitive to low-mass perturbers close to low-order mean-motion resonances. The RV data set limits masses of inner perturbers to $\sim$40 $M_{\rm Earth}$ for tightest orbits and to $\sim$70 $M_{\rm Earth}$ for orbits close to WASP-3b. The transit timing constrains masses of fictitious planets down to 1.7, 0.9, and 1.9 $M_{\rm Earth}$ in inner 3:1, 2:1, and 5:3 orbital resonances, respectively. For the outer perturbers, the RV method limits their masses down to $\sim$100 $M_{\rm Earth}$ for the most close-in orbits. The TTV method allows us to probe masses down to 2.6, 0.8, and 13 $M_{\rm Earth}$ in outer 5:3, 2:1, and 3:1 orbital resonances, respectively.

4. SUMMARY

We have acquired 32 new transit light curves for the planet WASP-3b, and 17 precise RV measurements for the WASP-3 host star. Our new data cover a timespan of 2 yr from 2009 to 2011. The tangible result of our study is refining stellar, orbital, and planetary parameters with improved precision. Our studies of the stellar activity of WASP-3 confirm its long timescale variation reported by Montalto et al. (2012) and also reveal a night-to-night variability when the star was in a more active state. These short timescale variations are likely to be caused by active regions that are carried around by stellar rotation.

Our result for the planetary mass ($M_b = 1.77^{+0.11}_{-0.09}\ M_{\rm Jup}$) agrees with the value reported by Pollacco et al. (2008), and the radius ($R_b = 1.346 \pm 0.063\ R_{\rm Jup}$) falls between estimates of Gibson et al. (2008) and Christiansen et al. (2011). Additional RV measurements provide tighter constraints on the orbital eccentricity ($e_b = 0.02 \pm 0.01$) than Pollacco et al. (2008). The orbit of WASP-3b is expected to be circular because its circularization timescale of 1–14 Myr for the tidal dissipation parameter Q_p between 10^5 and 10^6 is much shorter than the system's age of $3.9^{+1.3}_{-1.2}$ Gyr.

Despite all of this observational effort, no evidence for the presence of the additional planet in the WASP-3 system was found. Published hints for both periodic and chaotic variations in transit timing are likely caused by underestimated uncertainties and systematic effects affecting photometric measurements. We find a spectroscopic sign of variation in stellar activity for WASP-3 that is reported by Montalto et al. (2012). However, our high-precision photometry shows no evidence for starspot-crossing anomalies or other effects that stellar activity might have on transit light curves. The current precision of transit timing observations allows us to rule out Earth-mass planetary companions of WASP-3b near the lowest-order mean-motion resonances. The RV data show no sign of additional bodies, and in particular no long-term trend over a few years. We note, however, that the portion of parameter space for additional bodies that remains unexplored is still significant.

Analysis of a sample of hot Jupiter candidates observed with the *Kepler Space Telescope* (Borucki et al. 2010) shows that the overwhelming majority of these planets are devoid of close planetary companions (Latham et al. 2011; Steffen et al. 2012). This effect is interpreted as a result of the dynamical evolution of planetary systems containing close-in giant planets. In this context, a lack of confirmation of TTVs for WASP-3b is consistent with expectations arising from the *Kepler* survey.

REFERENCES

Adamów, M., Niedzielski, A., & Wolszczan, A. 2012, MSAIS, 22, 48
Borucki, W. J., Koch, D. G., Basri, G., et al. 2010, Sci, 327, 977
Bressan, A., Marigo, P., Girardi, L., et al. 2012, MNRAS, 427, 127
Carter, J. A., & Winn, J. N. 2009, ApJ, 704, 51
Carter, J. A., Winn, J. N., Holman, et al. 2011, ApJ, 730, 82
Chambers, J. E. 1999, MNRAS, 304, 793
Christiansen, J. L., Ballard, S., Charbonneau, D., et al. 2011, ApJ, 726, 94
Claret, A., & Bloemen, S. 2011, A&A, 529, A75
Csizmadia, Sz., Pasternacki, Th., Dreyer, C., et al. 2013, A&A, 549, A9
Cutri, R. M., Skrutskie, M. F., van Dyk, S., et al. 2003, yCat, 2246, 0
Eastman, J., Gaudi, B. S., & Agol, E. 2013, PASP, 125, 83
Eastman, J., Siverd, R., & Gaudi, B. S. 2010, PASP, 122, 935
Eibe, M. T., Cuesta, L., Ullán, A., Pérez-Verde, A., & Navas, J. 2012, MNRAS, 423, 1381
Fulton, B. J., Shporer, A., Winn, J. N., et al. 2011, AJ, 142, 84
Gazak, J. Z., Johnson, J. A., Tonry, J., et al. 2012, AdAst, 2012, 697967
Gibson, N. P., Pollacco, D., Simpson, E. K., et al. 2008, A&A, 492, 603
Gomes da Silva, J., Santos, N. C., Bonfils, X., et al. 2012, A&A, 541, A9
Høg, E., Fabricius, C., Makarov, V. V., et al. 2000, A&A, 355, L27
Howarth, I. D. 2011, MNRAS, 418, 1165
Hoyer, S., Rojo, P., & López-Morales, M. 2012, ApJ, 748, 22
Latham, D. W., Rowe, J. F., Quinn, S. N., et al. 2011, ApJL, 732, L24
Littlefield, C. 2011, arXiv:1106.4312
Lomb, N. R. 1976, Ap&SS, 39, 447
Maciejewski, G., Dimitrov, D., Neuhäuser, R., et al. 2010, MNRAS, 407, 2625
Maciejewski, G., Dimitrov, D., Seeliger, M., et al. 2013, A&A, 551, A108
Mandel, K., & Agol, E. 2002, ApJL, 580, L171
McLaughlin, D. B. 1924, ApJ, 60, 22
Meschiari, S., Wolf, A. S., Rivera, E., et al. 2009, PASP, 121, 1016
Miller, G. R. M., Collier Cameron, A., Simpson, E. K., et al. 2010, A&A, 523, A52
Molaro, P., & Monai, S. 2012, A&A, 544, A125
Montalto, M., Gregorio, J., Boué, A., et al. 2012, MNRAS, 427, 2757
Mugrauer, M., & Berthold, T. 2010, AN, 331, 449
Nascimbeni, V., Cunial, A., Murabito, S., et al. 2013, A&A, 549, A30
Neuhäuser, R., Errmann, R., Berndt, A., et al. 2011, AN, 332, 547
Niedzielski, A., Wolszczan, A., Nowak, G., et al. 2011, in IAU Symp. 276, The Astrophysics of Planetary Systems: Formation, Structure, and Dynamical Evolution, ed. A. Sozzetti, M. G. Lattanzi, & A. P. Boss (Cambridge: Cambridge Univ. Press), 445
Nowak, G., Wolszczan, A., Niedzielski, A., Adamów, M., & Maciejewski, G. 2013, ApJ, 770, 53
Pollacco, D., Skillen, I., Collier Cameron, A., et al. 2008, MNRAS, 385, 1576
Ramírez, I., & Meléndez, J. 2005, ApJ, 626, 465
Ramsey, L. W., Adams, M. T., Barnes, T. G., et al. 1998, Proc. SPIE, 3352, 34
Robertson, P., Endl, M., Cochran, W. D., & Dodson-Robinson, S. E. 2013, ApJ, 764, 3
Rossiter, R. A. 1924, ApJ, 60, 15
Sada, P. V., Deming, D., Jennings, D. E., et al. 2012, PASP, 124, 212
Scargle, J. D. 1982, ApJ, 263, 835
Schneider, J. 2000, in ASP Conf. Ser. 212, From Giant Planets to Cool Stars, ed. C. A. Griffith & M. S. Marley (San Francisco, CA: ASP), 284
Sestito, P., & Randich, S. 2005, A&A, 442, 615
Silva, A. 2003, ApJL, 585, L147
Simpson, E. K., Pollacco, D., Hébrard, G., et al. 2010, MNRAS, 405, 1867
Sousa, S. G., Santos, N. C., Israelian, G., Mayor, M., & Monteiro, M. J. P. F. G. 2007, A&A, 469, 783
Southworth, J., Maxted, P. F. L., & Smalley, B. 2004a, MNRAS, 349, 547
Southworth, J., Maxted, P. F. L., & Smalley, B. 2004b, MNRAS, 351, 1277
Steffen, J. H., Ragozzine, D., & Fabrycky, D. C. 2012, PNAS, 109, 7982
Straizys, V., & Kuriliene, G. 1981, Ap&SS, 80, 353
Stumpff, P. 1980, A&AS, 41, 1
Takeda, Y., Ohkubo, M., & Sadakane, K. 2002, PASJ, 54, 451
Takeda, Y., Ohkubo, M., Sato, B., Kambe, E., & Sadakane, K. 2005, PASJ, 57, 27
Torres, G., Fischer, D. A., Sozzetti, A., et al. 2012, ApJ, 757, 161
Tripathi, A., Winn, J. N., Johnson, J. A., et al. 2010, ApJ, 715, 421
Tull, R. G. 1998, Proc. SPIE, 3355, 387
Valenti, J. A., & Piskunov, N. 1996, A&AS, 118, 595
Zhao, M., Milburn, J., Barman, T., et al. 2012, ApJ, 748, 8